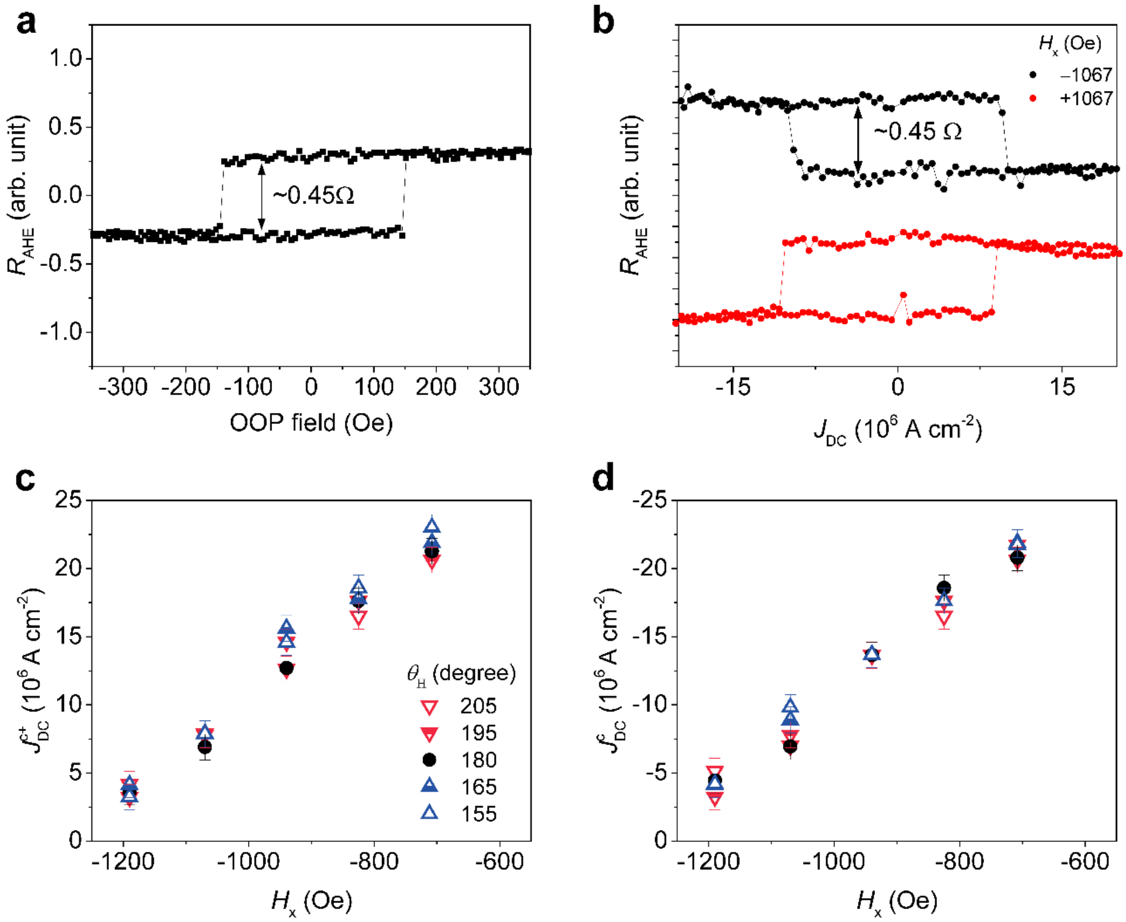


**Supplementary Figure 1. DC-current induced spin-orbit torque switching** (a) Anomalous Hall resistance ($R_{AHE}$) of patterned structure under out-of-plane external fields. (b) DC-current induced spin-orbit switching with respect to the assist-field polarity. (c) The critical switching current density from 'up' to 'down' state under DC-currents as a function of assist-field magnitude and field angle. (d) The critical switching current density from 'down' to 'up' state under DC-currents as a function of assist-field magnitude and field angle. Error bars indicate the standard deviation from several measurements.

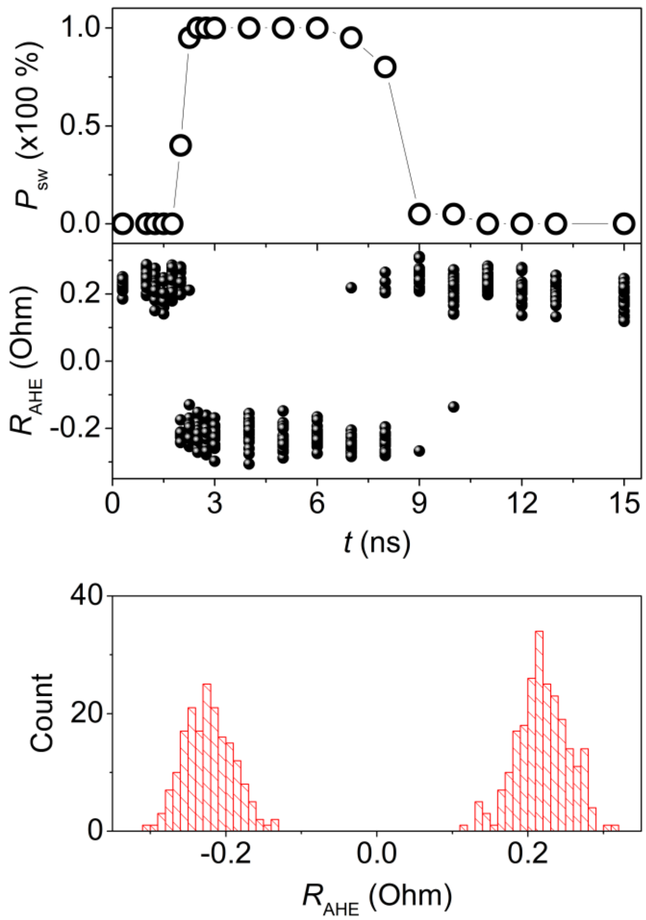


**Supplementary Figure 2. Reversal of PMA circular dot under current pulses** (a) The measured switching probability and its corresponding anomalous Hall resistance measurement result. Applied *J* and *H* are 64.3 $\times 10^6$ A $cm^{-2}$ and 1191 Oe, respectively. (b) Histogram of anomalous Hall resistance measurements.

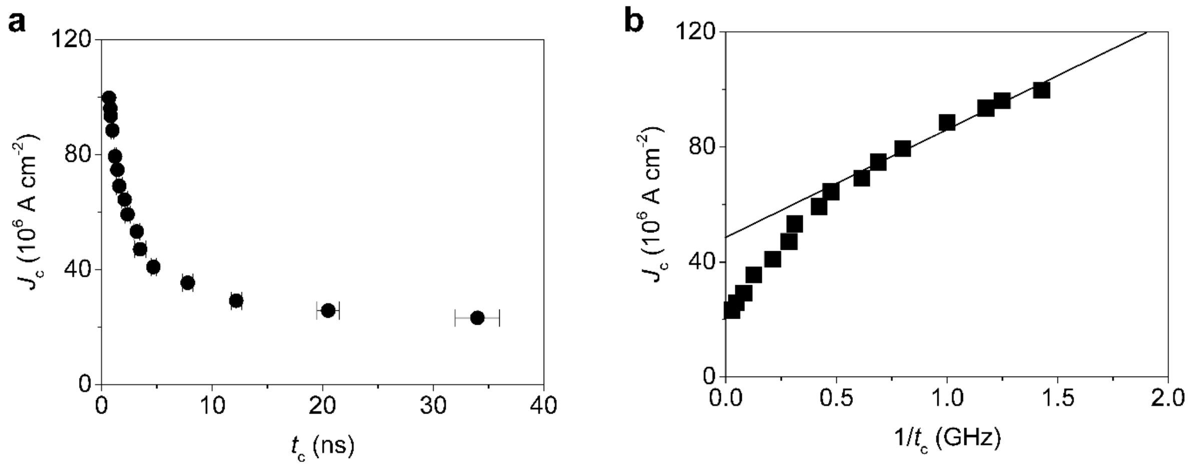


**Supplementary Figure 3. Estimation of the intrinsic critical switching current density** (a) The measured critical switching current density and its corresponding time scale from the current pulse switching under an assist-field of 1191 Oe. (b) The critical switching current density as a function of $1/t_c$. Error bars indicate the standard deviation from several measurements.

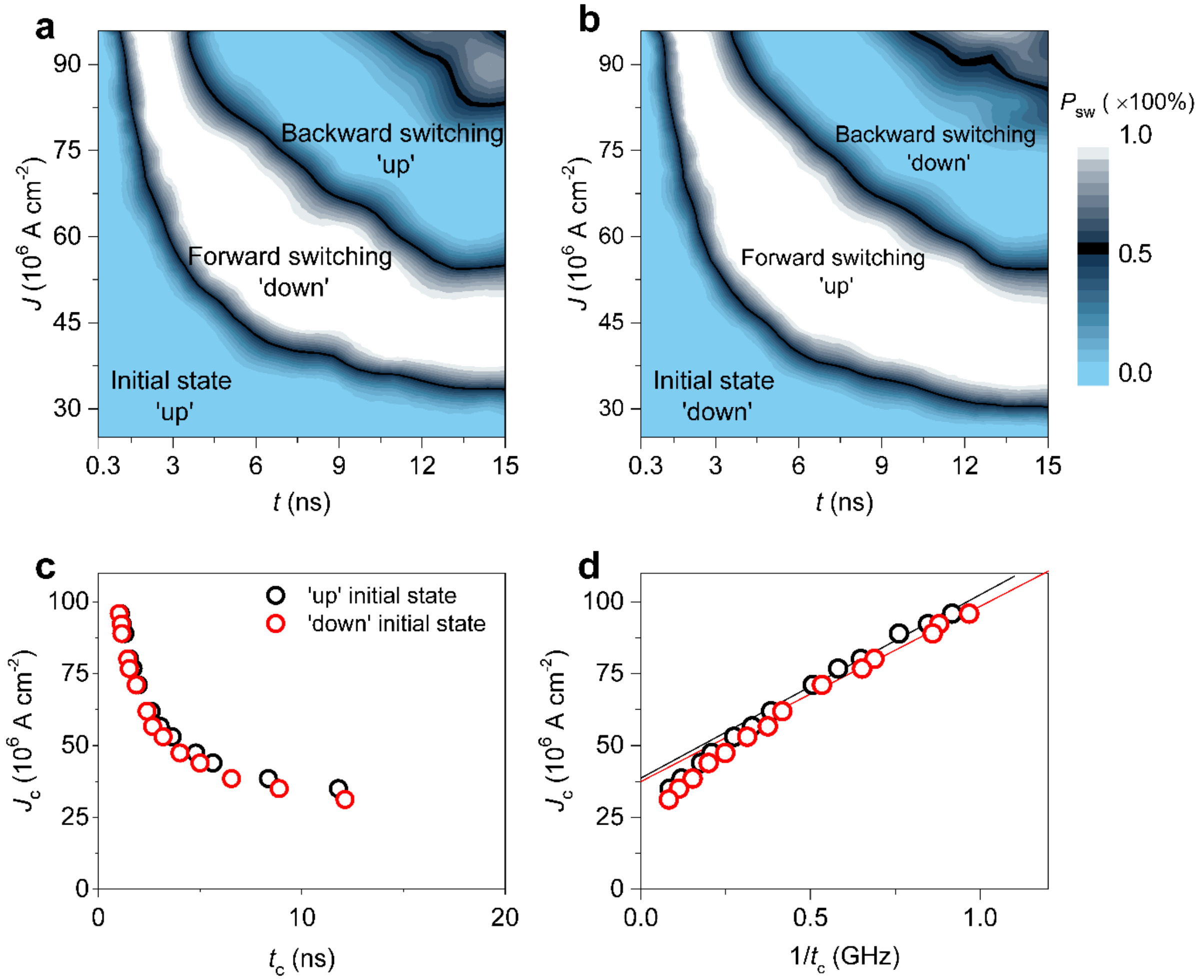


**Supplementary Figure 4. Nanosecond current pulse induced spin-orbit torque switching with different initial states** Spin-orbit torque switching in a Ta/CoFeB/MgO structure with different initial states. Switching probability diagrams with respect to $J$ and $t$, with (a) 'up' initial state and (b) 'down' initial state. (c) The measured critical switching current density and its corresponding time scale from the current pulse switching with two different initial magnetization directions. (d) The critical switching current density as a function of $1/t_c$. In-plane assist fields of $H_x$ = −1321 Oe and $H_x$ +1321 Oe were used for the 'up' initial state and 'down' initial state, respectively.

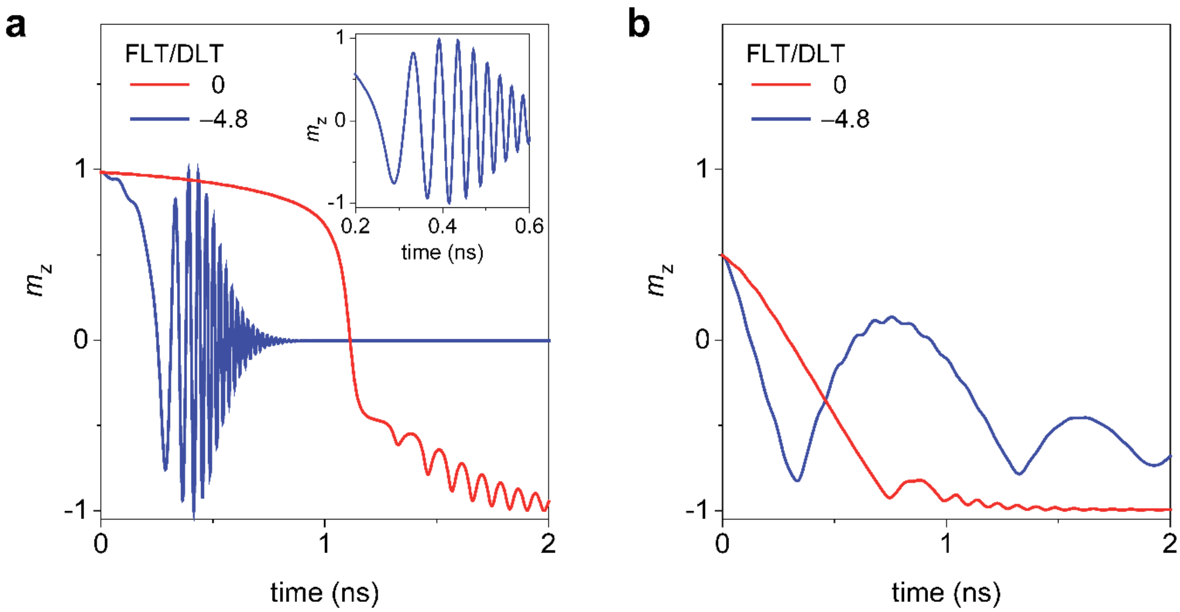


**Supplementary Figure 5. Oscillatory switching behavior in a single domain system** Micromagnetics simulation results showing the temporal evolution of out-of-plane magnetization during spin-orbit torque switching via (a) coherent magnetization rotation and (b) expansion of reversed domain (the data are from Fig. 2d). The inset in (a) shows a magnified region of the results with FLT/DLT = –4.8.

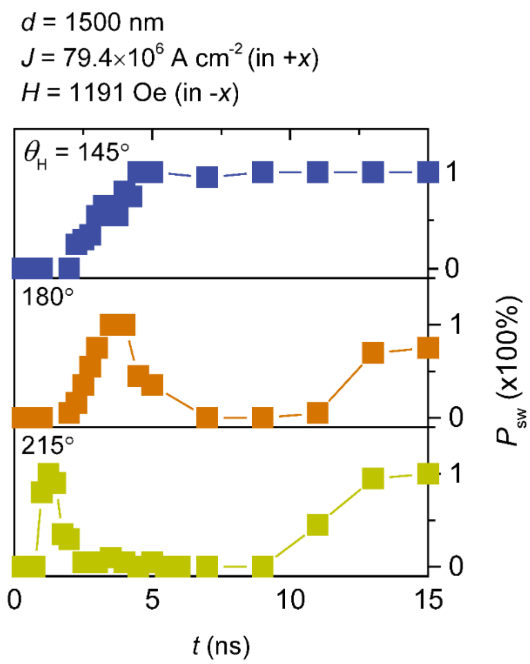


**Supplementary Figure 6. Complete suppression of the backward switching** The measured switching probability of a device with 1500 nm diameter as a function of in-plane angle ($\theta_H$) of the assist-field. The applied $J$ and $H$ are 79.4 $\times 10^6$ A cm$^{-2}$ and 1191 Oe, respectively.

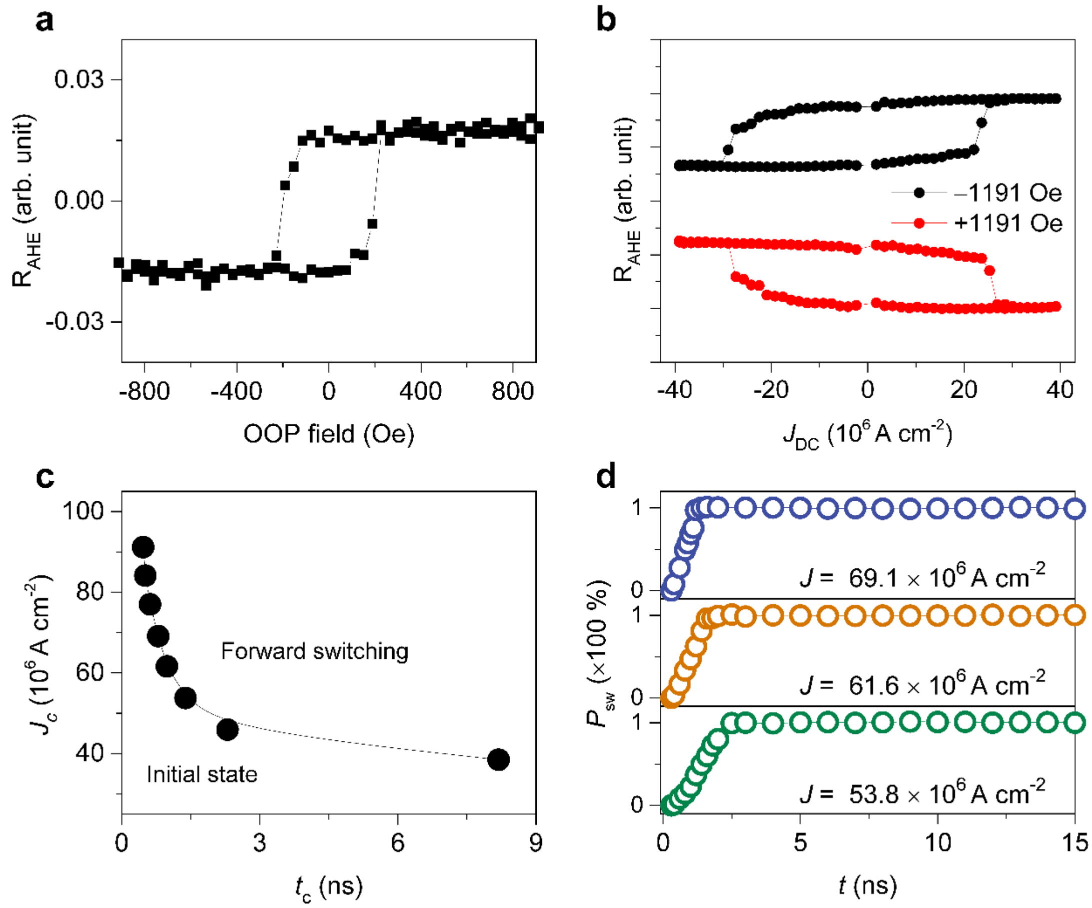


**Supplementary Figure 7. Spin-orbit torque switching in a Pt layer based device** Spin-orbit torque switching in the Pt/CoGd/$TaO_x$ structure which exhibits a small FLT/DLT ratio. (a) Anomalous Hall resistance of patterned structure under out-of-plane magnetic field. (b) DC-current induced spin-orbit torque switching with respect to the assist-field polarity. (c) The measured critical switching current density and its corresponding time scale from the current pulse switching under an assist-field of –1191 Oe. (d) The switching probability as a function of pulse duration with varying the current density under an assist-field of –1191 Oe.

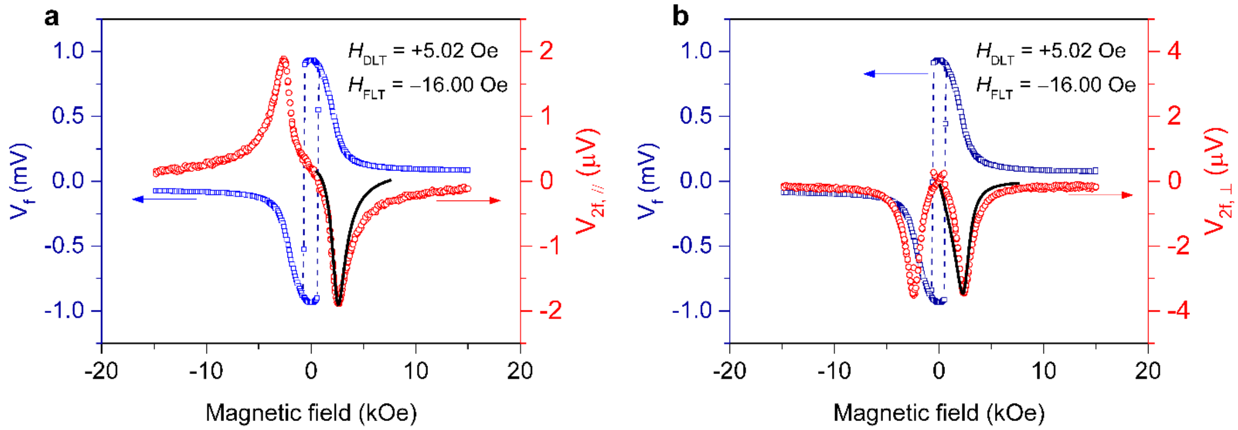


**Supplementary Figure 8. Effective spin-orbit torque fields measurements** First and second harmonic voltage under (a) longitudinal and (b) transverse magnetic fields. The $H_{DLT}$ and $H_{FLT}$ are estimated from the fitted curves (solid lines).

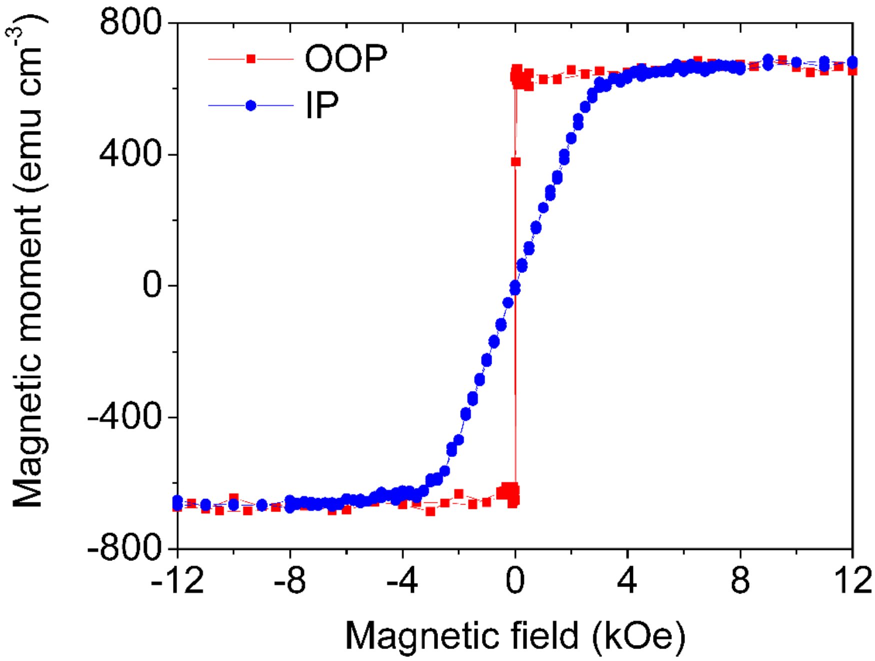


**Supplementary Figure 9. Vibrating sample magnetometer measurement** Measured *M*-*H* curve of un-patterned film of Ta (6 nm)/$Co_{40}Fe_{40}B_{20}$ (0.9 nm)/MgO (2 nm)/$SiO_2$ (3 nm) under in-plane (IP) and out-of-plane (OOP) fields.

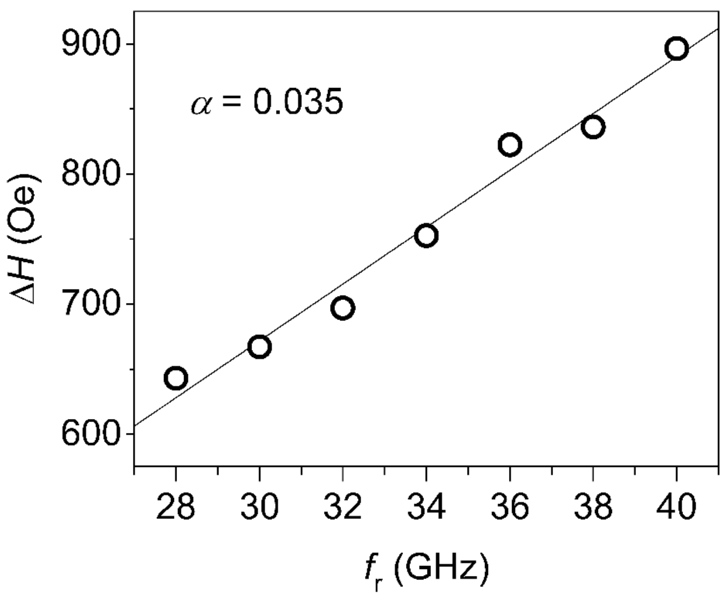


**Supplementary Figure 10. Ferromagnetic resonance measurements** Resonant frequency dependent FMR linewidth for the Ta/CoFeB/MgO film annealed at 200 °C for 30 minutes. Solid line is the linear fit.

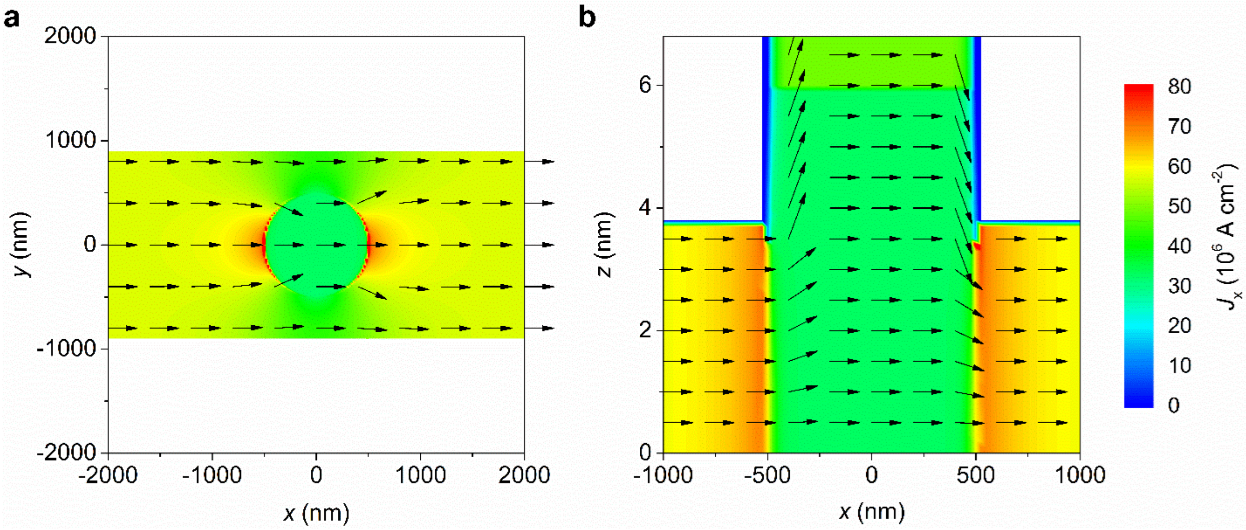


**Supplementary Figure 11. Calculated current distribution in the device** (a) Top view and (b) cross-sectional view of the calculated current distribution in the patterned device. The colored contours show the results current density projection along the *x*-axis and the arrows indicate the results for the current flow route.

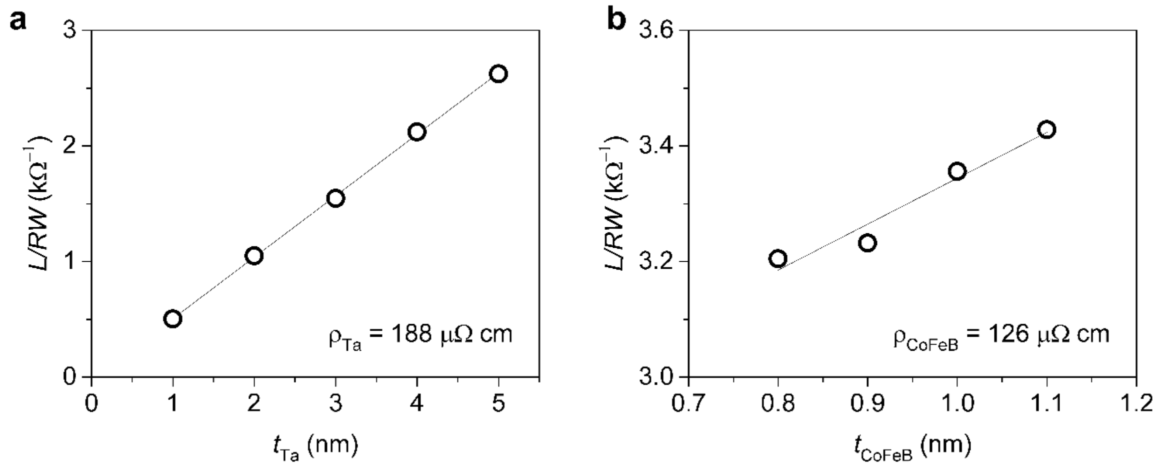


**Supplementary Figure 12. Resistivity measurements** Measured results for $L/(R \cdot W)$ as a function of (a) Ta layer thickness and (b) CoFeB layer thickness. The solid lines indicate linear fits.

**Supplementary Note 1. DC-current induced spin-orbit torque switching**

Supplementary Figure 1a shows the anomalous Hall resistance ($R_{AHE}$) under out-of-plane field from the same patterned device in the main manuscript. The patterned circular CoFeB dot shows clear perpendicular magnetic anisotropy (PMA), as the $R_{AHE}$ signal is proportional to the out-of-plane component of CoFeB magnetization. In our sign convention, the positive and negative $R_{AHE}$ indicates the magnetization pointing 'up' ($M_z > 0$) and 'down' ($M_z < 0$), respectively. Applying DC-currents into the Ta channel, under the in-plane assist-field collinear with the current-flow direction, results in deterministic switching of the PMA circular dot. As shown in Supplementary Figure 1b, the switching polarity depends on the direction of assist-field, which is a distinct feature of the spin-orbit torque induced switching. Under a negative field (the assist-field is applied opposite to the current-flow direction), the positive current switches the magnetization from 'up' to 'down', while 'down' to 'up' switching is observed under a positive field and positive current. The observed switching polarity is in agreement with previous reports on spin-orbit torque switching using a Ta channel[1-3]. The DC critical switching current density ($J_{DC}$) linearly decreases with increasing the magnitude of in-plane assist field as shown in Supplementary Figure 1c-1d. The observed decrease in the switching current density with respect to the field is attributed to a better alignment of the internal component at the center of domain wall to the field direction, which results in the increase in the DLT equivalent field experienced by the domain wall[4]. On the other hand, the $J_{DC}$ is kept nearly constant with respect to the in-plane angle ($\theta_H$) of assist-field as shown in Supplementary Figure 1c-1d, which implies a negligible change of the domain wall configuration in the static scenario.

**Supplementary Note 2. Reversal of PMA circular dot under current pulses**

Applying current pulses results in spin-orbit torque switching with a reversal of the PMA circular dot as in the DC-current induced switching. Supplementary Figure 2a shows measured anomalous Hall resistance ($R_{AHE}$) after series of current pulse injection from the same device in the main manuscript. The current pulses are applied along the +*x*-direction with a current density ($J$) of 64.3 $\times 10^6$ A cm$^{-2}$ and the in-plane assist field ($H$) is applied along the –*x*-direction ($\theta_H$ = 180°) with magnitude of 1191 Oe. A wide range of current pulse duration ($t$) is applied to observe the oscillatory switching behavior. The $R_{AHE}$ change after the forward ('up' to 'down') and backward ('down' to 'up') switching is ~0.45Ω, which is in agreement with the value achieved from DC-current measurements as shown in Supplementary Note 1. This result indicates that full switching of the PMA circular dot is achieved in both the forward and backward switching under current pulses. Supplementary Figure 2b shows the histogram of measured $R_{AHE}$ in Supplementary Figure 2a.

**Supplementary Note 3. Estimation of the intrinsic critical switching current density**

The intrinsic critical switching current density ($J_{c0}$) is a linear fit of the switching current density ($J_c$) with its corresponding time scale ($t_c$). The $t_c$ is the required time to achieve the forward switching, which is defined at $P_{sw}$ = 50%. Supplementary Figure 3a shows $J_c$ as a function of $t_c$ which was obtained from Fig. 1b in the main manuscript. The slope of switching boundary shows the well-known behavior of torque driven switching with thermal activation[5-6]. The switching boundary exhibits a strong dependence to $t_c$ in short time scale (< 3 ns) and weak relation to $t_c$ in relatively long time scale (>3 ns), which indicate spin-torque dominated switching and thermally activated switching regimes, respectively[5]. In the torque-dominated regime, the intrinsic critical switching current density ($J_{c0}$) is estimated to be 43.2 × $10^6$ A cm$^{-2}$ from the linear fit of $J_c$ to $1/t_c$, as shown in Supplementary Figure 3b.

**Supplementary Note 4. Pulse induced spin-orbit torque switching with different initial states**

The effect of initial magnetization direction on the oscillatory switching behaviors is investigated by measuring the switching probability diagram with different initial magnetization directions ('up' and 'down') and the results are shown in Supplementary Figure 4. The switching probability diagrams with 'up' initial state (Supplementary Figure 4a) and 'down' initial state (Supplementary Figure 4b) are quite similar, and both show the backward switching as well as the oscillatory switching behavior. This result suggests that the DW configurations during the forward and backward switching are mainly governed by the assist-field[4] and the FLT equivalent field as described in the main manuscript. The $J_{c0}$ is estimated to be 38.6 × $10^6$ A $cm^{-2}$ ('up' initial state) and 37.5× $10^6$ A $cm^{-2}$ ('down' initial state) from the linear fit of $J_c$ to $1/t_c$. The comparable magnitude of $J_{c0}$ from two different initial magnetization directions suggests that the tiling of equilibrium magnetization, and thus, the effects of higher-order anisotropy are negligible in our studied structure[7-8]. The device used in Supplementary Figure 4 is fabricated using different batch of films and shows a slightly higher depinning field and switching current density compared to that used in the main manuscript.

**Supplementary Note 5. Micromagnetics study on the oscillatory switching behavior in a single domain system**

The spin-orbit torque induced switching behavior in a single domain system is investigated by solving the Landau–Lifshitz–Gilbert equation as described in the main manuscript and the results are shown in Supplementary Figure 5a. Following parameters are used: the saturation magnetization $M_s$ = 670 emu $cm^{-3}$, the perpendicular anisotropy $K$ = 3.83 × $10^6$ erg/$cm^3$, the damping $\alpha$ = 0.035, the DLT efficiency $c_{DLT}$ = –0.09, and the FLT efficiency $c_{FLT}$ = 0 or +0.43. The considered geometry has dimension of 20 nm × 20 nm × 2 nm and was not divided into multiple unit cells. The current pulse with a current density of 950× $10^6$ A $cm^{-2}$, a rise time of 1 ns, and a duration of 10 ns is applied along the +$x$-direction, while the in-plane assist field with a magnitude of 1000 Oe is applied along the –$x$-direction.

Without considering the FLT (FLT/DLT = 0), the magnetization switches from up ($m_z$ = +1) to down ($m_z$ = –1) state via simple rotational motion. The magnetization precession about $m_z$ = 0 is not observed as the DLT does not directly compete with the damping torque[9]. However, when a considerable FLT is taken together with the DLT (FLT/DLT = –4.8), the magnetization exhibits precession motion about $m_z$ = 0. The FLT generates an effective field, which is orthogonal to the current flow direction ($x$) and the thickness direction ($z$). Therefore the magnetization exhibits large precession about the $y$-axis and $m_z$ shows oscillation over time[10], which is similar to the field-induced switching dynamics under a transverse field[11-12]. As the time varying magnetization trajectory oscillates between the two potential minima ($m_z$ = +1 or –1), the oscillatory switching behavior can be also achieved from the single domain case.

The oscillatory switching behavior can arise both from the coherent rotational switching (Supplementary Figure 5a) and the domain expansion switching (Supplementary Figure 5b). However, the two switching models show a distinct difference in the oscillation period. In the case of rotational switching (single domain), the period of oscillatory switching is quite short (< 0.1 ns) and symmetric as it arises from the precessional motion with a constant frequency (~ Larmor frequency). On the other hand, the oscillatory behavior in the domain expansion switching shows a rather longer (~1 ns) and asymmetric period between the forward and backward switching, as the switching time is governed by the lateral dimension of the device and the DW speed which is different during the forward and backward switching.

**Supplementary Note 6. Complete suppression of the backward switching**

Supplementary Figure 6 shows the measured switching probability ($P_{sw}$) of another device with a 1500 nm diameter circular dot. The film structure is identical to the device in the main manuscript. The applied $J$ and $H$ are 79.4 $\times 10^6$ A cm$^{-2}$ and 1191 Oe, respectively. When the applied $H$ is along the –$x$-direction ($\theta_H$ = 180°), measured $P_{sw}$ shows an oscillatory behavior with respect to $t$. The forward 'up' to 'down' switching (transition of $P_{sw}$ from 0 % to 100 %) is observed with application of relatively short current pulses. If we apply a longer current pulses, a backward switching appears (transition of $P_{sw}$ from 100 % to 0 %) where the magnetization flips back from 'down' to its initial 'up' state and followed by another 'up to 'down' forward switching. The backward switching is completely suppressed as the $H$ is tilted towards ($\theta_H$ < 180°) the +$y$-direction as the measured $P_{sw}$ is remained at 100% with increasing $t$. On the other hand, the backward switching is enhanced as the $H$ is tilted away ($\theta_H$ > 180°) from the +$y$-direction. The harmonic Hall voltage measurements in the Ta/CoFeB/MgO structure have shown that a large $H_{FLT}$ exists in the –$y$-direction when a positive current (along the +$x$-direction) is applied[13-14]. The backward switching is suppressed when the effective $H_{FLT}$ is reduced by applying an external transverse field along the +$y$-direction ($\theta_H$ < 180°) opposite to the SOT induced $H_{FLT}$ (along the –$y$-direction) as discussed in the main manuscript.

**Supplementary Note 7. Spin-orbit torque switching in a Pt layer based device with a small FLT/DLT ratio**

The film structure of Pt (8 nm)/$Co_{79}Gd_{21}$ (5 nm)/$TaO_x$ (1 nm)/$SiO_2$ (3 nm) on a Si/$SiO_2$ substrate is prepared by magnetron sputtering (base pressure < $1 \times 10^{-8}$ Torr) and subsequently patterned into a PMA circular dot with a 1000 nm diameter following the same procedure in the main manuscript. The FLT/DLT ratio is estimated to be −0.5 which is much smaller than that from the Ta/CoFeB/MgO structure (see Supplementary Note 8).

The patterned CoGd dot shows clear PMA as shown in Supplementary Figure 7a. Applying DC-currents into the Pt channel, under the in-plane assist-field collinear with the current-flow direction, results in deterministic switching of the PMA circular dot as shown in Supplementary Figure 7b. Under a negative field (the assist-field is applied opposite to the current-flow direction), the positive current switches the magnetization from 'down' to 'up', while 'up' to 'down' switching is observed under a positive field and positive current, which are in agreement with previous reports on spin-orbit torque switching using a Pt channel[4, 6, 15]. We have measured the $P_{sw}$ by applying current pulses at a fixed $H = -1191$ Oe and the results are shown in Supplementary Figure 7c and 7d. We estimate $J_{c0}$ as $36.5 \times 10^6$ A cm$^{-2}$ from a linear fit of $J_c$ with $1/t_c$. The results of $P_{sw}(t)$ in the spin-torque dominated switching regime ($J > J_{c0}$) are plotted in Supplementary Figure 7d. In contrast to the Ta/CoFeB/MgO structure in the main manuscript, the $P_{sw}$ remains at 100 % and does not change with increasing $t$ after the switching occurs. This is expected from the small FLT/DLT ratio in the Pt/CoGd/$TaO_x$ structure and clearly indicates that FLT plays a dominant role in breaking the determinism in SOT switching dynamics.

**Supplementary Note 8. Spin-orbit torque effective fields measurements**

The spin-orbit torque fields are quantified using the harmonic technique[13-14, 16-17]. The Ta (6 nm)/$Co_{40}Fe_{40}B_{20}$ (0.9 nm)/MgO (2 nm)/$SiO_2$ (3 nm) structure is annealed at 200 °C for 30 minutes and patterned into Hall bar. A sinusoidal current $I_{ac}$ with the amplitude of 400 μA and the frequency of 13.7 Hz is applied to the Hall bars, and the first and second harmonic signals are measured by sweeping a magnetic fields in the longitudinal ($V_{/\!/}$) and transverse direction ($V_{\perp}$) with respect to the current flow direction. The second harmonic signal is fitted following the model in Ref. 14 and the results are shown in Supplementary Figure 8. With accounting the planar Hall effect, we estimate $H_{DLT}$ and $H_{FLT}$ as +5.02 Oe (corresponding to +496 Oe per $10^8$ A cm$^{-2}$) and

−16 Oe (corresponding to −1583 Oe per $10^8$ A $cm^{-2}$). The sign of SOT fields is consistent with previous reports[13-14] and the corresponding FLT/DLT ratio is −3.2. The DLT efficiency $c_{DLT}$ (akin to the spin Hall angle) and FLT efficiency $c_{FLT}$ is estimated as −0.09 and +0.29, respectively, from the following relation; $c_{DLT(FLT)} = (2e/\hbar) M_s t_{FM} H_{DLT(FLT)} / J$ , where $e$ is the electron charge, $\hbar$ is the reduced Plank's constant, $M_s$ is the saturation magnetization (670 emu/$cm^3$), and $t_{FM}$ is the ferromagnetic layer thickness (0.9 nm). The effective spin-orbit torque fields in the Pt (8 nm)/$Co_{79}Gd_{21}$ (5 nm)/$TaO_x$ (1 nm)/$SiO_2$ (3 nm) structure are measured using the same procedure. The effective $H_{DLT}$ and $H_{FLT}$ are estimated as −15.82 Oe and +7.75 Oe, respectively, using the sinusoidal current $I_{ac}$ with the amplitude of 1 mA and the frequency of 13.7 Hz. The corresponding FLT/DLT ratio is −0.5.

**Supplementary Note 9. Characterization of magnetic film**

The saturation magnetization ($M_s$) and effective anisotropy field ($H_{k,eff}$) are determined from *M*-*H* loops measured by a vibrating sample magnetometer (VSM). Supplementary Figure 9 shows the measured VSM result of un-patterned film of Ta (6 nm)/$Co_{40}Fe_{40}B_{20}$ (0.9 nm)/MgO (2 nm)/$SiO_2$ (3 nm) under in-plane (IP) and out-of-plane field (OOP). The film was annealed at 200 °C for 30 minutes and shows clear perpendicular magnetic anisotropy. The measured $M_s$ and $H_{k,eff}$ values are 670 emu $cm^{-3}$ and 3000 Oe, respectively, which gives a perpendicular anisotropy energy density ($K = 0.5M_sH_{k,eff} + 2\pi M_s^2$) value of $3.83 \times 10^6$ erg $cm^{-3}$.

**Supplementary Note 10. Magnetic damping measurement**

The damping constant of annealed Ta (6 nm)/$Co_{40}Fe_{40}B_{20}$ (0.9 nm)/MgO (2 nm)/$SiO_2$ (3 nm) film is estimated from the field swept ferromagnetic resonance spectroscopy (FMR). Supplementary Figure 10 shows the measured FMR linewidth ($\Delta H$) as a function of the resonant frequency ($f_r$). The damping constant is estimated as 0.035 from the following formula[18]

$\Delta H = \Delta H_0 + 4\pi\alpha f_r / \gamma$. Here, $\Delta H_0$ is the inhomogeneous linewidth broadening, $\alpha$ is the Gilbert damping constant, and $\gamma$ is the gyromagnetic constant.

**Supplementary Note 11. Current distribution in the patterned device**

The current density distribution in our patterned device is studied with the finite element method by using COMSOL multiphysics. The studied structure consists of two conducting layers of Ta and CoFeB with the thickness of 6 nm and 0.9 nm, respectively. The thickness of the Ta channel after fabrication is 3.5 nm, estimated from channel resistance measurements. We considered the calculation in a three-dimensional problem with geometry parameters from the actual patterned device. In the electric current problem, the current density is determined as the current conservation with $\nabla \cdot J = Qj$ and Ohm's law with $\vec{J} = \sigma\vec{E}$. The following boundary conditions are used; the perpendicular component of the current density is zero at the surface with $\vec{J} \cdot \vec{n} = 0$, and the in-plane component of current is zero with $\vec{J} \cdot \vec{n} = \pm j_0$ at the left/right sides which represents the current flow in and out. The electrical conductivities of Ta and CoFeB layers are $5.32 \times 10^5$ S/m and $7.94 \times 10^5$ S/m respectively, obtained from the resistivity measurements with varying Ta and CoFeB layer thicknesses (see Supplementary Note 12). The calculated results are shown in Supplementary Figure 11 with a (a) top view and a (b) cross-sectional view. The current in the Ta layer is quite uniform in the lateral plane, but slightly shunted to the CoFeB layer in the thickness direction which is responsible for the anomalous Hall resistance.

**Supplementary Note 12. Resistivity of Ta and CoFeB layers**

The resistivity of Ta and CoFeB layer are evaluated using the four-probe method. We prepared Ta ($t_{Ta}$)/$Co_{40}Fe_{40}B_{20}$ (0.9 nm)/MgO (2 nm)/$SiO_2$ (3 nm) and Ta (6 nm)/$Co_{40}Fe_{40}B_{20}$ ($t_{CoFeB}$)/MgO (2 nm)/$SiO_2$ (3 nm) structures and annealed at 200 °C for 30 minutes. Supplementary

Figure 12 shows the results of normalized inverse channel resistance ($L/(R \cdot W)$) as a function of $t_{Ta}$ and $t_{CoFeB}$. Here, $L$ is the channel length and $W$ is the channel width. By fitting a linear function, we estimate the resistivity of Ta and CoFeB layers as 188 μΩ cm and 124 μΩ cm, respectively.

**Supplementary References**


1. Zhang, C. *et al.* Magnetization reversal induced by in-plane current in Ta/CoFeB/MgO structures with perpendicular magnetic easy axis. *J. Appl. Phys.* **115,** 17C714 (2014).
2. Lo Conte, R. *et al.* Spin-orbit torque-driven magnetization switching and thermal effects studied in Ta\CoFeB\MgO nanowires. *Appl. Phys. Lett.* **105,** 122404 (2014).
3. Liu, L. *et al.* Spin-Torque Switching with the Giant Spin Hall Effect of Tantalum. *Science* **336,** 555-558 (2012).
4. Lee, O. J. *et al.* Central role of domain wall depinning for perpendicular magnetization switching driven by spin torque from the spin Hall effect. *Phys. Rev. B* **89,** 024418 (2014).
5. Liu, H. *et al.* Dynamics of spin torque switching in all-perpendicular spin valve nanopillars. *J. Magn. Magn. Mater.* **358–359,** 233-258 (2014).
6. Garello, K. *et al.* Ultrafast magnetization switching by spin-orbit torques. *Appl. Phys. Lett.* **105,** 212402 (2014).
7. You, L. *et al.* Switching of perpendicularly polarized nanomagnets with spin orbit torque without an external magnetic field by engineering a tilted anisotropy. *Proceedings of the National Academy of Sciences* **112,** 10310-10315 (2015).
8. Torrejon, J. *et al.* Current-driven asymmetric magnetization switching in perpendicularly magnetized CoFeB/MgO heterostructures. *Phys. Rev. B* **91,** 214434 (2015).
9. Lee, K.-S., Lee, S.-W., Min, B.-C. & Lee, K.-J. Threshold current for switching of a perpendicular magnetic layer induced by spin Hall effect. *Appl. Phys. Lett.* **102,** 112410 (2013).
10. Legrand, W., Ramaswamy, R., Mishra, R. & Yang, H. Coherent Subnanosecond Switching of Perpendicular Magnetization by the Fieldlike Spin-Orbit Torque without an External Magnetic Field. *Phys. Rev. Appl.* **3,** 064012 (2015).
11. Lee, J. M. & Lim, S. H. An alternate switching/non-switching behavior of a nanostructured magnetic thin film under sub-Stoner-Wohlfarth switching fields. *J. Appl. Phys.* **110,** 093910 (2011).
12. Schumacher, H. W. *et al.* Phase Coherent Precessional Magnetization Reversal in Microscopic Spin Valve Elements. *Phys. Rev. Lett.* **90,** 017201 (2003).
13. Garello, K. *et al.* Symmetry and magnitude of spin-orbit torques in ferromagnetic heterostructures. *Nat. Nanotech.* **8,** 587-593 (2013).
14. Qiu, X. *et al.* Angular and temperature dependence of current induced spin-orbit effective fields in Ta/CoFeB/MgO nanowires. *Sci. Rep.* **4,** 4491 (2014).
15. Miron, I. M. *et al.* Perpendicular switching of a single ferromagnetic layer induced by in-plane current injection. *Nature* **476,** 189-193 (2011).
16. Pi, U. H. *et al.* Tilting of the spin orientation induced by Rashba effect in ferromagnetic metal layer. *Appl. Phys. Lett.* **97,** 162507 (2010).
17. Jamali, M. *et al.* Spin-Orbit Torques in Co/Pd Multilayer Nanowires. *Phys. Rev. Lett.* **111,** 246602 (2013).
18. Kalarickal, S. S. *et al.* Ferromagnetic resonance linewidth in metallic thin films: Comparison of measurement methods. *J. Appl. Phys.* **99,** 093909 (2006).